



A plastic scintillator-based muon tomography system with an integrated muon spectrometer

V. Anghel^a, J. Armitage^b, F. Baig^a, K. Boniface^a, K. Boudjemline^b, J. Bueno^c, E. Charles^d, P.-L. Drouin^e, A. Erlandson^{b,a,*}, G. Gallant^d, R. Gazit^c, D. Godin^a, V.V. Golovko^a, C. Howard^e, R. Hydromako^{c,e}, C. Jewett^a, G. Jonkmans^{a,e}, Z. Liu^c, A. Robichaud^b, T.J. Stocki^f, M. Thompson^a, D. Waller^{e,**}

^a Canadian Nuclear Laboratories Ltd (former Atomic Energy of Canada Ltd), Chalk River Laboratories, Chalk River, Canada K0J 1P0

^b Department of Physics, Room 3302 Herzberg Laboratories, Carleton University, 1125 Colonel By Drive, Ottawa, Canada K1S 5B6

^c Advanced Applied Physics Solutions Inc., 4004 Wesbrook Mall, Vancouver, Canada V6T 2A3

^d Canada Border Services Agency, 79 Bentley Avenue, Ottawa, Canada K1A 0L8

^e Defence Research and Development Canada, 3701 Carling Avenue, Ottawa, Canada K1A 0Z4

^f Radiation Protection Bureau, Health Canada, 775 Brookfield Rd, AL6302D, Ottawa, Canada K1A 0K9

ARTICLE INFO

Article history:

Received 6 February 2015

Received in revised form

26 June 2015

Accepted 29 June 2015

Available online 3 July 2015

Keywords:

Cosmic-ray muon

Multiple Coulomb scattering

Tomography

Large-volume inspection

Muon tomography

Scintillation detector

ABSTRACT

A muon scattering tomography system which uses extruded plastic scintillator bars for muon tracking and a dedicated muon spectrometer that measures scattering through steel slabs has been constructed and successfully tested. The atmospheric muon detection efficiency is measured to be 97% per plane on average and the average intrinsic hit resolution is 2.5 mm. In addition to creating a variety of three-dimensional images of objects of interest, a quantitative study has been carried out to investigate the impact of including muon momentum measurements when attempting to detect high-density, high-Z material. As expected, the addition of momentum information improves the performance of the system. For a fixed data-taking time of 60 s and a fixed false positive fraction, the probability to detect a target increases when momentum information is used. This is the first demonstration of the use of muon momentum information from dedicated spectrometer measurements in muon scattering tomography.

Crown Copyright © 2015 Published by Elsevier B.V. This is an open access article under the CC BY-NC-ND license (<http://creativecommons.org/licenses/by-nc-nd/4.0/>).

1. Introduction

The smuggling of special nuclear material (SNM) or radiological sources is a significant security concern. Detection of these materials at ports-of-entry can be challenging when the materials are heavily shielded. One potential solution to this challenge is to use muon scattering tomography (MST) to detect high-density, high-Z material (e.g. uranium and plutonium metals, or dense shielding material) [1–3]. In MST, an object (e.g. a cargo container, nuclear waste drum(s), and spent nuclear fuel container(s)) is scanned for suspicious contents by comparing the trajectories of atmospheric muons (secondary particles produced by cosmic-ray interactions in the upper atmosphere) before and after they

traverse the object. Passage through a dense, high-Z material will tend to perturb the trajectory of a muon via multiple Coulomb scattering (MCS) more than less-dense, low-Z material. The planar projection of the scattering angles is modelled well by a Gaussian. The width of the Gaussian that approximates the distribution of MCS angles, ϑ_{MS} , is given by the Moliere formula [4]:

$$\vartheta_{MS} = \frac{13.6 \text{ MeV}}{\beta c p} \sqrt{\frac{L}{X_0}} \left\{ 1 + 0.038 \ln \left(\frac{L}{X_0} \right) \right\} \quad (1)$$

where β is the muon speed as a fraction of the speed of light, c , p is the muon momentum in MeV/c, L is the path length of the muon through the material (in g/cm²), and X_0 is the radiation length of the material (also in g/cm²). As MCS is affected by p , if one wants to determine the type of material causing the scattering, effectively by determining X_0 , then it is desirable to measure not just the scattering angle and L , but also p .

A MST system called Cosmic-Ray Inspection and Passive Tomography (CRIPT) has been constructed which uses extruded plastic scintillator bars for muon tracking and a dedicated muon spectrometer that measures scattering through steel slabs. This is the first

* Corresponding author at: Canadian Nuclear Laboratories Ltd, Chalk River Laboratories, Chalk River, Canada K0J 1P0.

Tel.: +1 613 584 3311x43982; fax: +1 613 584 8198.

** Corresponding author.

E-mail addresses: Andrew.Erlandson@cnl.ca (A. Erlandson), david.waller@drdc-rddc.gc.ca (D. Waller).

MST system to use this muon detection technology; other MST systems have employed either drift tubes [5–7], drift chambers [6], scintillating fibres [8], gas electron multipliers (GEMs) [9], or resistive plate chambers [10,11].

Section 2 of this paper provides details of the construction and commissioning of the CRIPT system, including descriptions of the plastic scintillator detectors, support tower and custom electronics. Section 3 describes the algorithms used for muon hit estimation, track finding, and momentum calculation. After this, Section 4 summarizes CRIPT's performance based on (1) muon detection efficiency, (2) hit and angular resolution, (3) momentum resolution, and (4) high-Z material detection with and without momentum information. To the best of our knowledge, this is the first use of “direc”¹ momentum measurements by an MST system.

2. The CRIPT detector

2.1. Geometry and construction

The CRIPT detection system, shown in Fig. 1, stands 5.3 m tall and employs three muon detection modules – the upper tracker (UT), lower tracker (LT) and spectrometer (SPEC) – each consisting of two position-sensitive detector super-layers. A super-layer is the combination of two individual layers of bars in perpendicular directions. The super-layers are each $2\text{ m} \times 2\text{ m}$ in area, constricting the geometrical acceptance for muons passing through all six detectors to a maximum zenith angle of 29.5° . In the UT and LT modules, these super-layers are separated by a vertical distance of 1 m and in the SPEC module they are separated by 0.5 m.

The entire structure weighs 19.4 metric tonnes with a large portion of this weight being situated in the spectrometer in the form of two, 10 cm thick, steel slabs (shown in yellow in Fig. 1 (left)). These slabs are interleaved between the two spectrometer super-layers so that the magnitude of muon scattering through the steel can be measured and used for the purpose of momentum estimation. The CRIPT spectrometer was designed to take advantage of the known measured spectrum of cosmic-ray muons from the BESS spectrometer [13].

The large CRIPT prototype system is based on a small prototype detector which used 1.00 m long, plastic scintillating bars for muon detection. The scintillation light is propagated along the length of the bars to photomultiplier tubes (PMTs) via wavelength-shifting (WLS) plastic optical fibres (POFs). The bars have a triangular cross-section (shown in Fig. 2) with a base width of $3.23 \pm 0.01\text{ cm}$, a height of $1.70 \pm 0.01\text{ cm}$ and an extrusion hole diameter of 2.4 mm for POF insertion. Each super-layer consists of two horizontal planes of 121 bars, positioned orthogonally with respect to one another. The two planes are independent, enabling the super-layer to measure an x and y coordinate for each detected muon event (called x -bar and y -bar signals respectively).

The scintillator is made of polystyrene infused with PPO (1% by weight) and POPOP (0.03% by weight) as fluors [14,15].² The bars were co-extruded at Fermilab with an exterior $250\text{ }\mu\text{m}$ coating of titanium dioxide (TiO_2) paint which helps us to internally reflect the predominantly ultraviolet (UV) and blue scintillation light produced by ionizing radiation. Each of the bars was cut to a length of 2 m, after which the ends were wet-sanded with fine-grit sand paper, polished to a transparent finish and coated with TiO_2 paint.

A 1.2 mm diameter Y11 Kuraray WLS POF is situated inside each of the extruded holes to convert the light to green light for propagation to individual pixels of a 64-channel Hamamatsu H8804 PMT [16]. A PMT assembly is shown in Fig. 3. The non-PMT end of each WLS POF has a vacuum-deposited aluminum mirror on it to reflect the light, thereby increasing the number of photons detected by the PMT. The ends of the fibres were then coated with an epoxy to protect the mirror finish.

Each individual plane is divided into two sections consisting of 60 or 61 bars, each having its own POF holder and PMT assembly. The fibre holders were machined to have 64 holes which line up with the center of each pixel on the PMT window. The configuration of bars-to-PMTs in each plane is shown in Fig. 4. The length of each fibre ranges from 2.7 m in the central bars and 3.8 m in the outermost bars and were chosen to ensure that no fibre will bend near its critical radius on its path from the scintillator to the PMT. The large prototype involves a single bend of the fibres to reach the PMT assembly whereas the small prototype had 2 bends.

To minimize the effect of crosstalk between neighbouring PMT pixels, a bar-to-pixel map was carefully chosen. This ensures that fibres in adjacent bars are not located side-by-side on the PMT window. Both the probability and the magnitude of crosstalk are maximum for pixels immediately beside or above the pixel in question but there is still a non-zero probability of crosstalk for pixels neighbouring on the diagonal.

The detector modules required extensive light shielding due to their sensitivity to ambient light. Each super-layer was fitted with two light-tight boxes to cover the electronics and WLS fibres protruding from the scintillation bars. The rest of the surfaces of the detector modules were covered with large-area foam-core material.

2.2. Data acquisition system and electronics

2.2.1. General description

The structure of the CRIPT data acquisition (DAQ) hardware is shown in Fig. 5. The DAQ system processes the pulses generated by the PMTs and records the results on a local PC. A front-end card (FEC) containing analog-to-digital converters (ADCs) continuously samples the PMT outputs and searches for a photon trigger event (PTE) (defined as the voltage level of an incoming analogue pulse crossing a programmable threshold). An Ethernet based slow control communication channel allows the PC to monitor the system behaviour and modify the configurable parameters.

Each PTE is packed into a short data stream containing (a) a series of ADC samples encapsulating the PTE, (b) the unique address of the specific channel, and (c) a global time stamp representing the exact time at which the event occurred.

A muon within the angular acceptance of a detector module should produce x -bar and y -bar signals in both super-layers of the module simultaneously. All data streams from each module (UT, LT, SPEC) are fed through high-speed proprietary digital links into a local collector card that can detect and suppress non-simultaneous events. Data streams from the three local collector cards are fed to a global collector that sorts the multiple data streams using the time stamp and identifies coincidence events by looking for data streams from all super-layers that share a given time window. The global collector makes decisions based on inputs generated by the FECs, at the super-layer level (that are passed through the local collectors). This procedure is crucial in order to reduce the overall data throughput; samples that do not have matching signals throughout the detector are ignored. The coincidence operation happens online, without the introduction of dead time, thereby maximizing the coincidence event detection. Coincidence events are sent over a standard Gigabit Ethernet link for storage and subsequent offline post-processing on a PC.

¹ An indirect measurement of muon momenta has been published in [12] which measure the scattering of a muon in the inspection volume to estimate the momentum.

² The fluors are (1) POP (2,5-diphenyloxazole) and (2) POPOP (1,4-bis-(2-(5-phenyloxazolyl))) benzene.

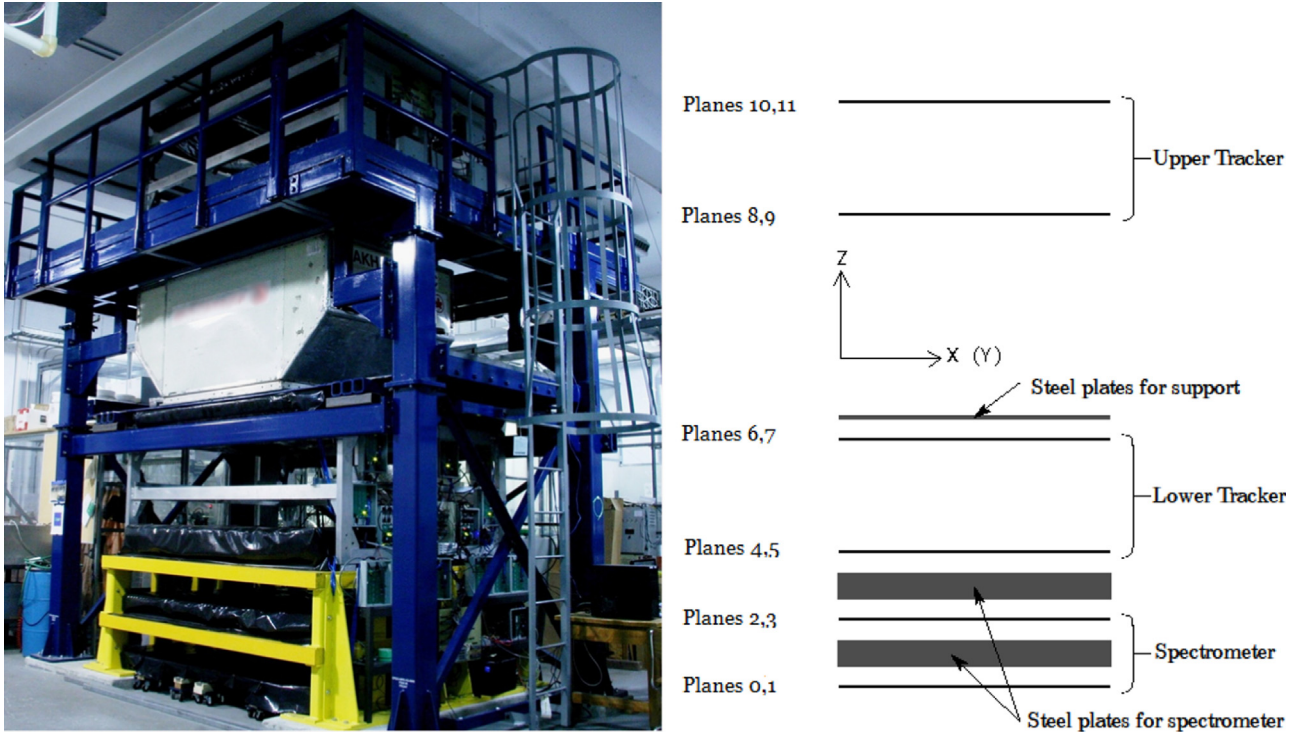


Fig. 1. Left: the Cosmic-Ray Inspection and Passive Tomography (CRIPT) detector with cargo container in the scanning area. Right: simplified diagram of particle tracking detectors and spectrometer. (For interpretation of the references to color in this figure, the reader is referred to the web version of this paper.)

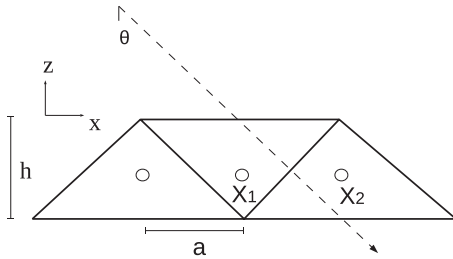


Fig. 2. Cross-sectional views of scintillator bars. The diagram shows the variables for the dual-bar hit-position calculation (see Eq. (3)). Positions x_1 and x_2 are the centres of the scintillator bars along that x -axis. The pitch-width of the detector layer is $a=1.6$ cm, and the height of the bars is $h=1.7$ cm. The dashed line shows the trajectory of an incident muon, with θ being the (zenith) angle from vertical.

2.2.2. DAQ PC software

The DAQ PC software is based on a MIDAS (maximum integrated data acquisition system) [17] framework with several project-specific additions. Most significantly, several front-end processes were written to interface with, control, and read back the DAQ hardware and PMTs. Specifically, these processes are responsible for receiving data from the DAQ devices and PMTs and integrating that data into the MIDAS data-stream. Other front-end processes were created to monitor the status of the detector's PC and hardware devices. Finally, a number of interactive interfaces were created to control the operation of the individual hardware devices, such as the PMT voltages, read-back channel trigger thresholds, and coincidence filter parameters. The collected data are recorded in binary format using live compression, stored on local disks, and backed up at a remote site.

2.2.3. PMT control

The high voltage (HV) required to power the PMTs is provided by high voltage boards (HVBs) and controlled by a proprietary slow control bus (SCB) connected to the HVBs (Vertilon [18]). While the



Fig. 3. CRIPT PMT assembly. The (larger) sensor interface and (smaller) slow control cards are shown on the left and right sides respectively of the assembly. The black plastic (Delrin) PMT holder and fibre alignment cookie are on the left and right sides respectively of the assembly, behind the electronic cards.

HVBs host the DC-DC/HV step-up modules, current/voltage and temperature/humidity monitoring sensors, the control and monitoring of these signals is performed by an independent slow control (SC) card directly connected to the HVB. On the SC card, the MIDAS slow control bus (MSCB) is used for an independent data path to the HV control. This serial RS-485 bus implements a proprietary protocol that integrates with the MIDAS DAQ system. An additional MSCB/Ethernet interface provides a standard Ethernet communication to the SC cards.

2.2.4. Channel trigger

The DAQ relies on a self-triggering mechanism in which each channel, based on its own trigger criteria, will generate the samples to be pushed downstream. A programmable look-up table, implemented by the DAQ firmware, allows the arranging of channels into logical groups which are later used for coincidence detection to determine whether a trigger event occurred simultaneously on all the detector modules (and local collector cards).

2.2.5. FPGA firmware

Custom FPGA (field-programmable gated array) firmware was developed to support the CRIPT DAQ hardware. For the FECs, the FPGA firmware controls the read-back of the ADCs and provides a flexible and configurable interface for defining the per-channel ADC read-out conditions. Likewise, firmware on the local collector cards controls high-speed data paths and the communication links between the FECs and the collectors and between the global collector and the PC where the data are ultimately stored. The firmware for the local and global collector cards includes a highly configurable event coincidence algorithm which is used to select and record only muon-like tracks. The global collector card also implements a hardware user datagram protocol (UDP) offload mechanism to arrange the data into standard Gigabit Ethernet packets and send them to the PC through the same link that is used for slow controls and monitoring.

2.3. Monte Carlo modelling

The CRIPT detector has been modelled using GEANT4 [19], version 10.0. All standard electromagnetic physics are included.



Fig. 4. CRIPT scintillator bars and WLS fibres. Two 64-channel PMTs read out each layer of 121 bars. One of this layer's PMT holders is highlighted. It is coupled to the fibres from the upper 60 bars in this photo. The inset photo shows the 60 WLS fibres read-out by a (missing) PMT. The fibres from the lower 61 bars are read out by the other PMT.

The geometry as discussed in Section 2.1 has been converted from CAD drawings to ensure accuracy and that the proper materials were simulated. The simulation geometry is shown in Fig. 6. Each of the 1452 plastic scintillator bars, as well as their TiO_2 coatings, has been included. The thickness of this coating has been measured using calipers on cross-sections of random bars. The thickness of the TiO_2 coating is larger at the apexes. The size of this extra-thick TiO_2 coating was found to have a large effect on the ratio of single to multiple bar triggers on a given plane and was tuned within measurement uncertainty to best match the data.

Simulated events that pass the trigger criteria, as described in Section 2.2.4, have their energy deposition, bar number, and position of each interaction recorded. This information is then used in a separate custom simulation and analysis package, which accounts for PMT quantum efficiencies, photon attenuation lengths, and varying lengths of WLS POFs. The energy deposition is then converted to a charge in each bar for comparison to data.

2.4. Commissioning

2.4.1. PMT high voltage

Fig. 7 shows measurements of the average position resolution of each detector module as a function of the applied HV. It was determined that the position resolution of the system was optimized at an HV of -900 V. The vertical error bars result from the method used to calculate the individual layer position resolutions. The nominal resolution is taken as the arithmetic mean of these values. Since only very minor variations were observed in the range of 840 – 950 V it is assumed that the dependence of the average resolution on nominal applied HV is weak and therefore contributes negligibly to overall detector performance.

2.4.2. Normalizing detector response

A critical requirement for accurate hit finding in the CRIPT detector layers is to have a uniform response from each bar (or channel) in a single layer. Every channel in the CRIPT detector will have a slightly different response to interactions with ionizing

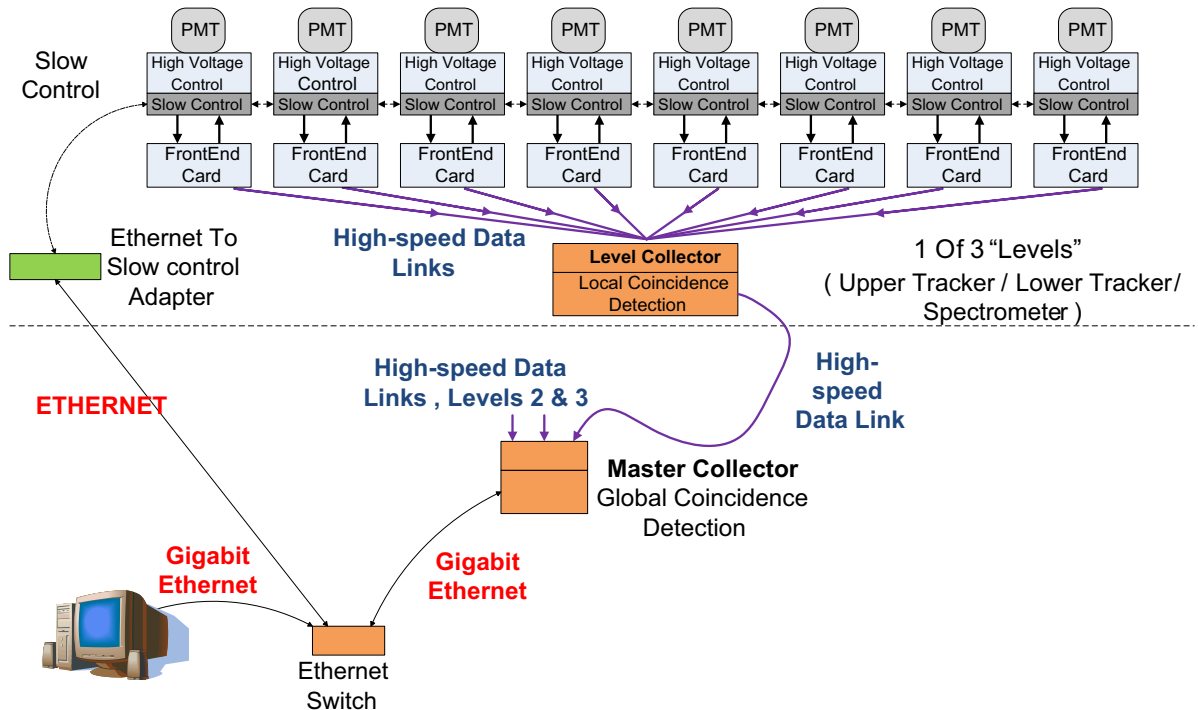


Fig. 5. DAQ hardware structure. The Master Collector connects to three Local Collectors. One Local Collector and its associated Front End Cards and PMTs are shown.

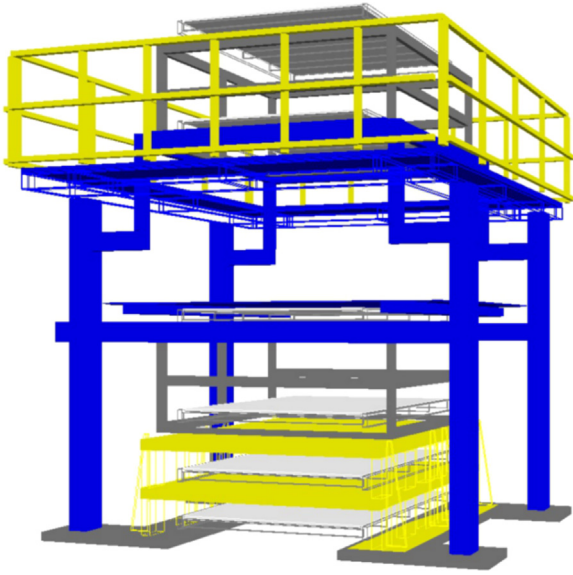


Fig. 6. The simulated geometry of CRIPT.

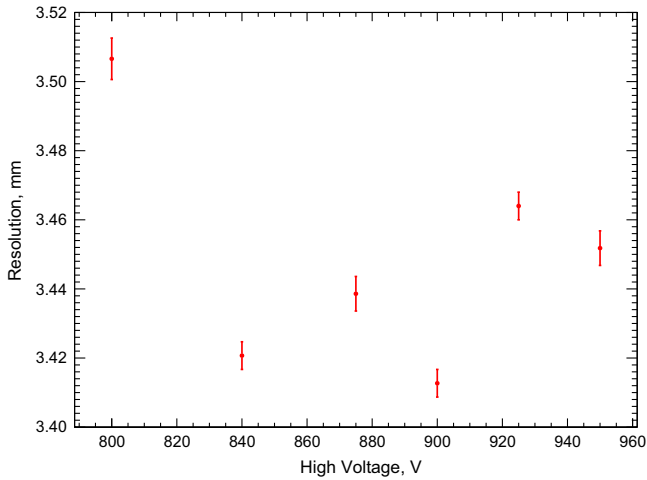


Fig. 7. Average position resolution versus applied high voltage.

particles. Factors affecting this are the production and transmission of scintillation photons, optical coupling to the WLS fibres, wavelength shifting and transport in the fibres, coupling to the photocathodes, gains of the PMTs, and gains and thresholds of the ADCs. In order to minimize bias in the determination of the particle position (and optimize the position resolution) the detector response is normalized channel-by-channel.

The charge, Q , normalization for the CRIPT detector modules is done at the software level after signals have been processed by the DAQ. The inverse charge distribution ($1/Q$) is plotted for each channel on a layer-by-layer basis and the low inverse charge events (predominantly due to atmospheric muons) are fit with a Landau function. An example of the fitted $1/Q$ distribution for one channel is shown in Fig. 8. The raw charges are then scaled so that the Most Probable Value (MPV) of the fitted Landau distributions is the same for each channel.

The calibrated and uncalibrated distributions of the mean charges collected by each bar are shown in Fig. 9. The bars are numbered consecutively by plane, so Bar Numbers 0–120 correspond to Detector Layer 0 (the bottom layer in the spectrometer), Bar Numbers 121–241 correspond to Detector Layer 1, and so on. There is a wave-like pattern in the raw charge values for each detector layer as the bars closer to the middle of each layer (e.g.

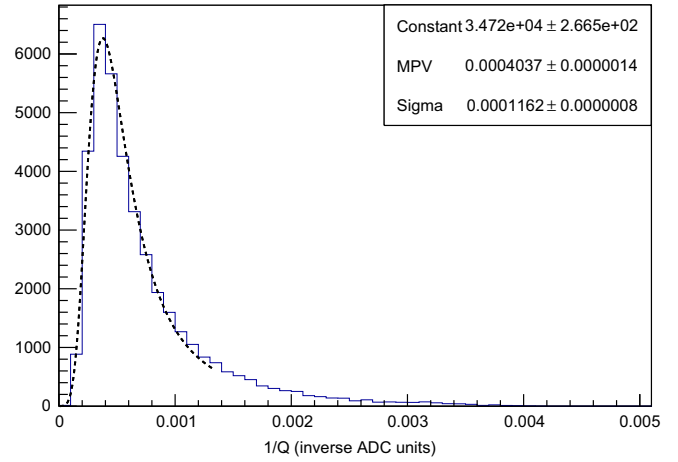


Fig. 8. The inverse charge, ($1/Q$), for each channel is fit with a Landau function as part of the calibration procedure. The Most Probable Value (MPV) of the raw charge is used to normalize the response of the channel.

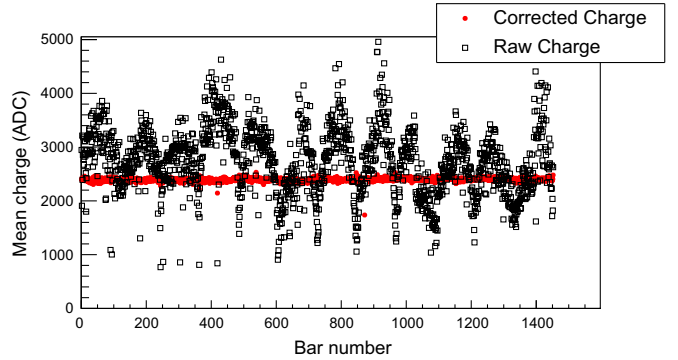


Fig. 9. Plot of the mean charge per channel with and without calibration (closed red circles are corrected charge and open black squares are raw charge). The total number of scintillating bars in the upper tracker, lower tracker and spectrometer is 1452. (For interpretation of the references to color in this figure caption, the reader is referred to the web version of this paper.)

Bar Number 60 for Detector Layer 0) tend to produce higher raw charge because central bars have shorter WLS fibre lengths (2.7 m versus 3.8 m for bars on the edges of a layer) so have reduced light attenuation. For less than 1% of the bars (the percentage varies from run to run), the calibrated mean charge does not converge to the nominal value; this is likely due to sub-optimal optical coupling which affects the fitting of the charge distribution for that channel. These bars are still retained for analysis as their data provide useful information (i.e. the tracking resolution would be worse if the bars' data were ignored).

2.4.3. Detector alignment

The detector layer positions were surveyed with a laser-alignment to serve as initial conditions for a software alignment using muon tracks. The software alignment was performed in two steps: first the horizontal (x and y co-ordinates) alignment was performed, then the vertical (z) alignment.

For the horizontal alignment, muon track data were acquired with no objects in the imaging volume (to minimize multiple scattering). Each muon track candidate that has hits in all 12 detector layers is fit by a straight line. Details of hit finding are provided in the next section. The set of horizontal displacements for each detector layer which minimizes an objective function, X^2 ,

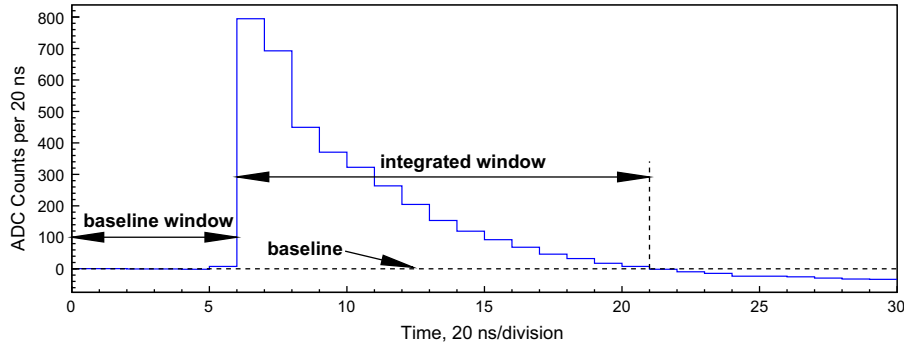


Fig. 10. Typical inverted digitized output pulse for a PMT signal.

is then determined. The objective function is defined as

$$X^2 = \sum_{i=0}^n \sum_{j=1}^{12} (x_{\text{Fit};i,j} - x_{\text{Measured};i,j})^2, \quad (2)$$

where i is the muon track candidate number, n is the total number of muon candidates, $x_{\text{Measured};i,j}$ is the position of the hit candidate for the j -th detector layer in its frame of reference, and $x_{\text{Fit};i,j}$ is the muon position in the frame of reference of the j -th plane found by the linear fit using the hit positions for the non- j planes. *Minuit* [23] is used to minimize the X^2 function. The best fit values for the horizontal displacements (from the nominal positions) varied from 0.8 to 8.3 mm. Possible rotations of the detector layers with respect to their nominal orientations were also considered in the alignment process, but were found to be negligible. The set of vertical displacements for each detector layer was determined in a similar, iterative fashion. Correcting the detector positions improves the measured position resolution of the detectors, indicating the success of the procedure.

3. Data analysis

3.1. Hit finding

The trajectory of an incident muon is sampled as the particle passes through each layer of scintillator bars, and the position of the traversal point is referred to as a ‘hit’. For the CRIPT geometry, the vertical position of each hit is fixed at the height of the mid-point of that layer within the detector apparatus; however, the scintillator bars cannot determine the position of the hit in the longitudinal coordinate along the bar. This means that a pair of scintillator layers (a super-layer) is required to determine the three-dimensional muon traversal point.

Fig. 10 shows a typical, muon-induced PMT pulse as recorded by the CRIPT DAQ system (note that the shape and duration of the pulse are largely set by shaping filters at the DAQ input). The integral of the waveform is proportional to the charge collected at the PMT anode and therefore proportional to the energy deposited by the through-going muon. An estimate of the PMT charge is obtained by summing the bins above the baseline (calculated by the mean of the first four ADC samples in the waveform). The integration window is determined by moving forward and backward from the peak of the waveform until the ADC samples cross the baseline in each direction (the overshoot in the late-time of the pulse is an artifact of the shaping filter and does not contribute to the charge calculation).

Referring to Fig. 2, for perfectly triangular bars, an incident cosmic-ray muon would be required to pass through at least two scintillator bars while traversing each plane. However, the active volume of the scintillator bars used in CRIPT does not extend all of

the way to the corners of each bar. This gap means that some muons pass through the active volume of only one scintillator bar in a layer. In those cases where only one scintillator bar in a plane registers a pulse, the trajectory of the muon is constrained to pass through the apex of the triangular bar.

When two adjacent scintillator bars register PMT pulses, the ratio of the charge values can be used to interpolate the hit position. Consider again Fig. 2, where the centre of the bar that is traversed first is x_1 , and the center of the second bar is x_2 ; the position of the hit along the x -axis, which is aligned with the vertical half-point of the plane, is given as

$$x = x_1 + a \frac{Q_2}{Q_1 + Q_2} + \frac{h}{2} \cdot \frac{Q_2 - Q_1}{Q_1 + Q_2} \cdot \tan \vartheta \quad (3)$$

where a is the distance between adjacent fibres (i.e. the pitch width), h is the height of a bar, ϑ is the angle of the particle trajectory from vertical, and Q_1 and Q_2 are the charge values of the first and second bars respectively. The third term is a geometrical correction to account for non-zero track angles³; however, since the track angle cannot be determined from a single plane, the hit positions must be fit iteratively in conjunction with the track angle determination (to be discussed in Section 3.2).

3.2. Track segment reconstruction

Scattering tomography measurements require knowledge of the cosmic ray muon trajectory, both before and after its passage through the target volume. For the CRIPT apparatus, the ‘before’ track segment is measured by the UT module while the ‘after’ segment is recorded in the LT.

Since the muon trajectory is sampled in orthogonal coordinates, the reconstruction of the track segments can be done independently in the x - z and y - z planes, giving the track angle parameters: $\vartheta_{x,i}$ and $\vartheta_{y,i}$. Here, the track parameters $\vartheta_{x,i}$ and $\vartheta_{y,i}$ give the x - z and y - z projections of the track angle from vertical for the i th detector module (UT or LT).

The track angle parameters and hit positions can be determined for each module by iteratively fitting for both simultaneously. That is, a track angle for a module is determined from $\vartheta_{x,i} = \arctan(\Delta x_i / \Delta z_i)$ coupled with Eq. (3). In order to solve both equations, an initial guess is made with the track angle parameter set to $\vartheta_{x,i} = 0$, and the hit positions from the scintillator bars which give the largest combined charge values are selected. The track angle and hit position calculations are alternated until both converge; this usually requires fewer than five iterations.

³ When a muon passes through the vertical half-point of a plane equidistant from x_1 and x_2 , regardless of zenith angle, the muon pathlengths through the two bars are equal (and, ideally, so are Q_1 and Q_2), therefore the third term is equal to zero in this case. In all other cases where $\vartheta \neq 0$, this term is non-zero.

For a small fraction of events, secondary particles can complicate the track finding by introducing extra hits that can mimic muon tracks. However, since the scattering of muons in the target volume will generally be very small, information from the UT and LT are combined to reject spurious hit candidates. The vast majority of muon trajectories form an approximately straight line through the UT and LT and as such, hit combinations that result in very large differences in the track angle ($> 5\sigma$) can safely be ignored.

Finally, the orthogonal x and y hit position coordinates can be combined to give a single three-dimensional estimate for the muon position in each super-layer. This information is used as succinct input to the three-dimensional imaging routines (see Section 4.4).

3.3. Momentum estimation

The CRIPT spectrometer is designed to provide an estimate of the momenta of atmospheric muons. Due to the angular acceptance of the CRIPT apparatus, 59% of muons that pass through the upper and lower trackers will also pass through the spectrometer detector layers. As described in Section 2.1, the momentum spectrometer is composed of two x - y scintillator super-layers, interleaved with 10 cm thick steel slabs.

Since the scattering depends inversely on the particle momentum (see Eq. (1)), by measuring the amount of scatter that a muon undergoes through the known thickness of steel, an estimate can be made for the muon momentum. A muon that passes through both spectrometer detector super-layers and steel slabs provides four independent, projected scattering angle measurements; projected scattering angles in orthogonal planes (x - z and y - z) are independent from each other so one obtains two independent scattering measurements for each scattering layer.

The estimate of the muon momentum utilizes a Bayesian maximum a posteriori method [20], wherein a likelihood function for the muon scattering, along with a prior distribution for the muon momentum distribution, is maximized to find a point-estimate of the muon momentum before it passed through the spectrometer. The energy loss of the muon in each of the steel slabs is accounted for in the estimate.

Two prior distributions were investigated for the muon momentum distribution: (a) the atmospheric cosmic-ray muon momentum distribution that was experimentally measured with the BESS spectrometer [13], and (b) a flat distribution from 0 to 1 TeV/c (i.e. effectively infinite). The flat prior was found to provide better numerical stability, so it was adopted; when using a flat prior, the momentum estimate is equivalent to a maximum likelihood fit.

4. Detector performance

The detector performance results obtained from the CRIPT apparatus are mainly focussed on measurements made by the UT and LT. The presence of the large steel slabs in the spectrometer makes the performance of the spectrometer's detectors difficult to decouple from the multiple scattering in the steel slab.

4.1. Detection efficiency

To measure the detection efficiency for a given detector layer, the imaging volume was left empty and the DAQ trigger condition was modified to exclude that layer from the strict inclusion. That is, only the seven other layers in the UT and LT are required for the trigger condition to be satisfied. Using this modified trigger condition, the detection efficiency, ε_i , for layer i is defined as the

number of good hit candidates recorded by layer i divided by the number of events expected (based on the muon trajectory measured in the other seven layers).

Fig. 11 shows the results of the layer-wise efficiency measurements. On average, the measured hit detection efficiency per layer is 97%. It should be noted that these overall efficiency numbers are the convolution of all of the sub-stages of the detector devices, including the emission efficiency of the scintillated photons in the bars, the collection efficiency of the wavelength-shifting fibers, the quantum efficiency of the PMTs, and the efficiency of the DAQ trigger condition ($< 1\%$ of events will experience FIFO (first in first out) buffer limitations, causing hits to be dropped during peak event-rates). For the majority of 'inefficient' events, hits were indeed found in the plane under study, however the measured hit position was found to be more than 30 cm from the expected position. Some of these events are possibly due to noise or large-angle scattering of the muon in the scintillator bars or in the supporting apparatus. Although there appears to be a linearly decreasing trend in the measured efficiencies for each tracker, whereby the upper-most detector layer in each tracker has the highest efficiency, there is no a priori reason for this to occur. The fact that both trackers have the same trend is likely a coincidence. Ultimately, the measured hit detection efficiency is more than sufficient for pursuing muon tomography investigations.

4.2. Hit position and angular resolution

An important figure of merit for the performance of the CRIPT detector is the hit position resolution. Following from Eq. (3), the quality of the hit position calculation is limited by how well the measured charge approximates the path length of the muon in the scintillator bars. The measured charge is influenced by a number of factors: non-uniform energy deposition in the scintillators, the light-yield of the scintillating material, the efficiency for scintillator photons to be converted in the WLS fibre, attenuation in the WLS fibres, the quantum efficiency and gain of the PMTs, and the performance of the associated electronics. The dominant source of uncertainty for the hit resolution is statistical (Poisson fluctuations in the number of photons detected in each PMT channel) [15]. Furthermore, since the hit position resolution affects the reconstructed track angle resolution, the quality of the final three-dimensional images is influenced by the precision and accuracy of the measured hit position.

4.2.1. Measured hit position resolution

An estimate of the hit position resolution can be found from the recorded data using only the measured hit positions. For this estimate, two linear fits are performed for each scintillator plane and for each event: the first fit includes all of the hits (for either the x or the y coordinates), while the second fit excludes any hits from the scintillator plane under study. Using the two fit results, the residual distributions are generated by compiling a histogram of the difference between the measured hit position and the interpolated position where the fit crosses the scintillator plane under study. The estimate for the measured hit position resolution for the i th plane $\sigma_{\text{measured},i}$ is given by the expression

$$\sigma_{\text{measured},i} = \sqrt{\sigma_{\text{included}} \cdot \sigma_{\text{excluded},i}} \quad (4)$$

where σ_{included} is the width of the residual position distribution using the linear fits with all of the hits included, and $\sigma_{\text{excluded},i}$ is the width of the residual position distribution excluding the hit from plane i [21]. Fig. 12 shows the measured position resolution values for the UT and LT modules; the residual distributions for the SPEC module are significantly broadened by MCS from the steel slabs, such that good estimates are difficult for the measured

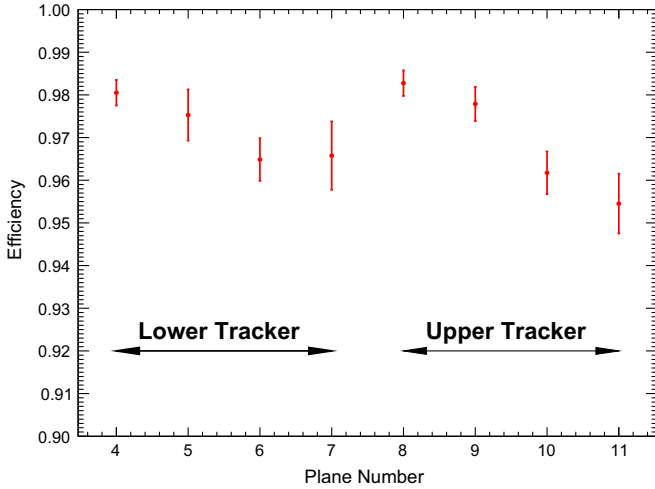


Fig. 11. Hit detection efficiency for the upper and lower trackers.

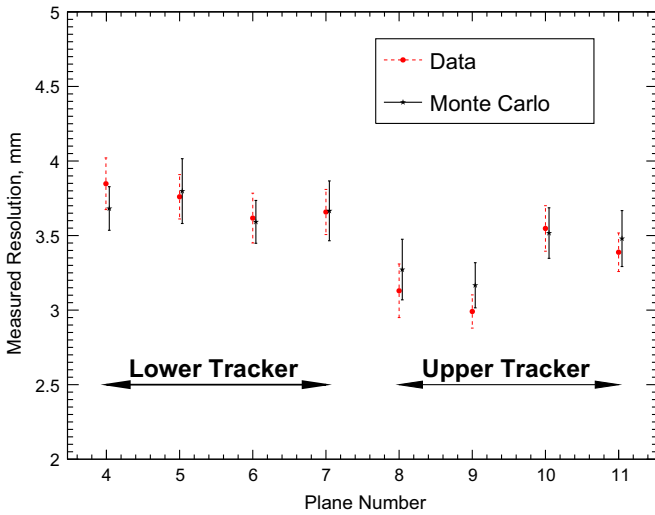


Fig. 12. The measured resolution values for the upper tracker and lower tracker, with the data values shown as the red, dashed bars with the circular markers and the Monte Carlo values shown as the black, solid bars with the star markers. (For interpretation of the references to color in this figure caption, the reader is referred to the web version of this paper.)

position resolutions. On average, the measured position resolution, including the effects of MCS, was found to be 3.5 mm.

4.2.2. Intrinsic hit position resolution

The linear fits used to measure the position resolution are affected by MCS within the scintillator bars and support apparatus. This results in the measured position resolution being an underestimate of how closely the measured hit position corresponds to the ‘true’ position where the muon passed through the scintillator bars.

The detailed Monte Carlo simulation described in Section 2.3 can be used to provide a position resolution estimate without the effects of MCS. Since the trajectory of the muon is known at every step during the Monte Carlo simulation, the ‘true’ position where a muon passes through a detector layer can be compared directly with the reconstructed hit position. However, the Monte Carlo simulation must first faithfully emulate the physical processes and details of the detector and DAQ system before reliable resolution values can be extracted. To this end, alongside the standard charge-transport and energy-deposition processes, the Monte

Carlo simulation also includes details about the WLS fibre attenuation, PMT quantum efficiency, DAQ gain and other parameters. These Monte Carlo parameters have been carefully tuned such that the simulation results closely match the observed data. Histograms of a number of variables were compared for Monte Carlo and data, and the Monte Carlo’s parameters were varied so that the Monte Carlo distributions were as similar as possible to the data distributions; the variables that were compared included

- the mean charges from all channels,
- the occupancies of all scintillator bars,
- the projected zenith angle distributions of muon track segments in the UT and LT,
- the ratio of muon hit candidates in each detector layer with one bar above threshold versus two adjacent bars above threshold, and
- the muon hit resolution (including MCS).

See Fig. 12 for an example of the comparison of the hit resolutions.

With the close correspondence between the observed and the Monte Carlo simulation, the intrinsic position resolution (that is, the position resolution without the influence of multiple scattering through the apparatus) can be extracted by directly comparing the ‘true’ position where the simulated cosmic-ray muon passed through the scintillator bars to the position calculated using the charge values and Eq. (3). Fig. 13 shows the comparison between the ‘true’ and calculated positions, along with a Gaussian fit to determine the width of the distribution.

From this fit, the intrinsic resolution is found to be 2.5 mm. It should be noted that this resolution value includes contributions from (a) hits with two adjacent scintillator bars (for which Eq. (3) can be applied), and (b) hits where only a single scintillator registered a charge value. The two-bar hits make up 81% of all hits while one-bar hits make up the remainder. The intrinsic resolution distribution with only single-bar hits has non-Gaussian tails and a width of 3.2 mm for the central Gaussian.

4.2.3. Angular resolution

Of paramount importance to the performance of a MST system is the angular resolution of the track measurements. The angular resolution depends on the hit resolution and the separation between the detector planes (or the lever arm). Since the

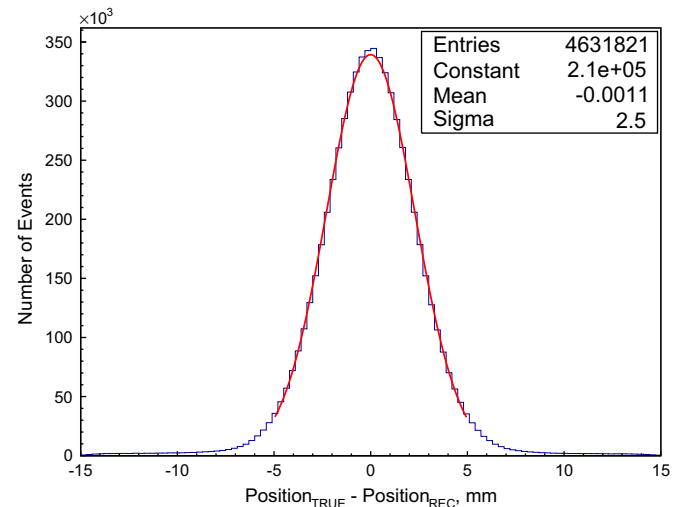


Fig. 13. The distribution of differences between the known position where the simulated cosmic-ray muons passed through the scintillation bars and the calculated hit positions using Eq. (3). The solid curve shows the Gaussian fit to the central region to find the distribution width.

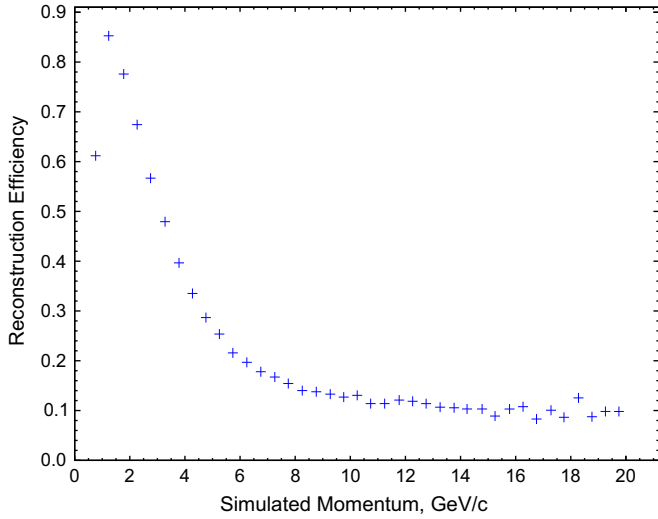


Fig. 14. The momentum reconstruction efficiency as a function of the simulated muon momentum.

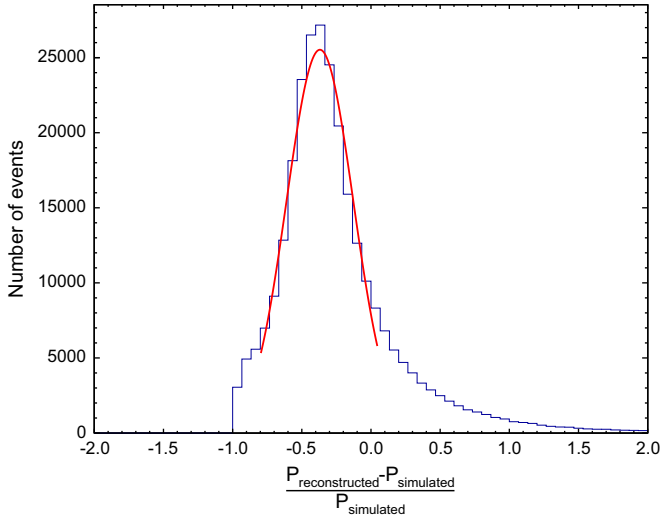


Fig. 15. The distribution of percent differences between simulated and reconstructed cosmic-ray muon momenta. The solid red curve shows a Gaussian fit to the central region of the distribution. (For interpretation of the references to color in this figure caption, the reader is referred to the web version of this paper.)

separation between the super-layers in each tracker is 1.0 m, the angular resolution of each tracker in the x - z plane, $\sigma_{\theta_{x,i}}$, is $\sqrt{2}\sigma_x/1000$ rad for vertical tracks where σ_x is the total (i.e. not intrinsic) hit resolution in mm, so $\sigma_{\theta_{x,i}} = 4.9$ mrad.⁴ The x - and y -hit resolutions are the same, so the angular resolutions in the x - z and y - z planes are also the same. The resolution for the x - z scattering angle measured in the imaging volume is $\sqrt{2}\sigma_{\theta_{x,i}}$ or 7.0 mrad. For a typical 3 GeV/c muon, the RMS scattering angle through 10 cm of steel is 11.9 mrad, while for 10 cm of uranium it is 28.0 mrad; the scattering angle resolution of the CRIPT system is small enough to discriminate these two materials.

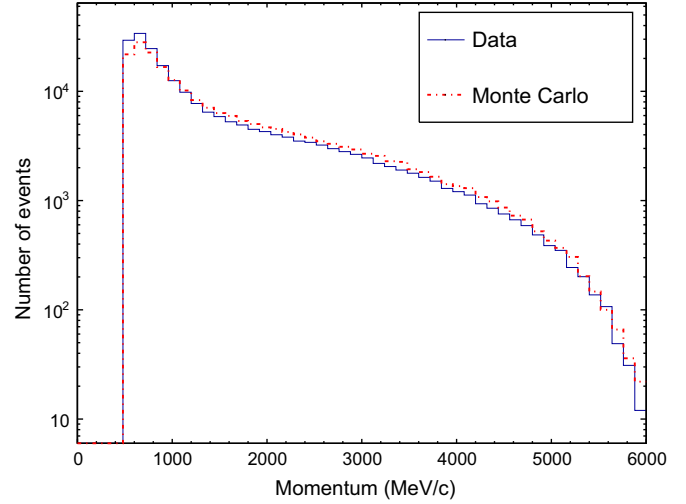


Fig. 16. No-target cosmic-ray muon reconstructed momentum spectra. The solid black trace shows the uncorrected, reconstructed momentum data collected over 3 h, while the dashed red trace gives the equivalent number of simulated Monte Carlo events (also uncorrected, reconstructed momentum).

Table 1

Mean and RMS of the momentum residuals as a function of the reconstructed muon momentum.

Reconstructed momentum (GeV/c)	Mean (%)	RMS (%)
$0.5 < p < 1.5$	−44.0	26.3
$1.5 < p < 3.0$	−11.4	43.9
$p > 3.0$	−3.2	67.5
All muons	−28.3	43.0

4.3. Momentum estimation results

4.3.1. Monte Carlo validation

The CRIPT Monte Carlo simulation, outlined in Section 2.3, is used to investigate the momentum estimation algorithm. Atmospheric muons, whose initial momenta are known (and follow the spectrum measured in [13]), are generated and their trajectories through the CRIPT apparatus are simulated. The momentum estimation algorithm (see Section 3.3) is run for simulated muons and the results are compared to the known (simulated) momentum. The algorithm converges for 49% of the simulated muons. For the vast majority of events with non-convergent momentum estimates, the muons do not scatter enough in the spectrometer steel slabs to have a measurable horizontal displacement in the detector super-layer immediately below (i.e. the horizontal displacement of the muon is comparable with or smaller than the hit resolution). These muons tend to have higher momenta than average: the median simulated momentum of muons whose momentum fits fail is 4.7 GeV/c compared to 1.8 GeV/c for those muons whose momentum fits converge. For muons with convergent momentum estimates, the Pearson correlation coefficient between the generated and reconstructed momenta is found to be 0.51, indicating a moderate degree of correlation which is useful for imaging (see Section 4.4).

Fig. 14 shows the probability for the muon momentum estimation algorithm to converge (the “reconstruction efficiency”) as a function of the generated momentum. Clearly, the algorithm is most likely to converge when the muon momentum is less than 3 GeV/c. Above 10 GeV/c, the efficiency is flat at approximately 12%. For muons whose fits fail to converge, a high momentum value can be assumed (e.g. 4.7 GeV/c, the median energy of these

⁴ For non-vertical muons (i.e. the zenith angle, θ , is non-zero) the muon hits in the detector layers are more than 1.0 m apart. In this case, $\sigma_{\theta_{x,i}} = \cos^2\theta\sqrt{2}\sigma_x/1000$.

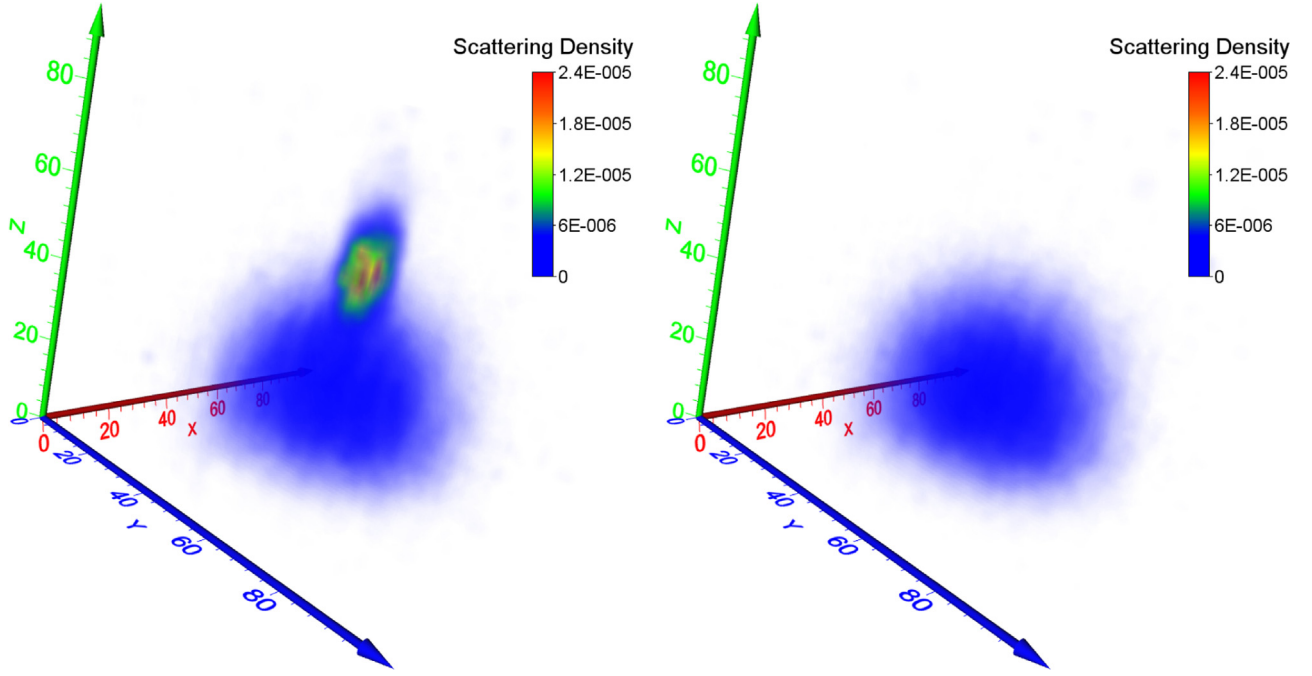


Fig. 17. Two 4.5 h scans: the left plot with 8000 cm^3 lead present, the right plot without lead. The color scale is scattering density in arbitrary units and the axes are in voxel number. The voxel dimensions are $2 \times 2 \times 2 \text{ cm}^3$. (For interpretation of the references to color in this figure caption, the reader is referred to the web version of this paper.)

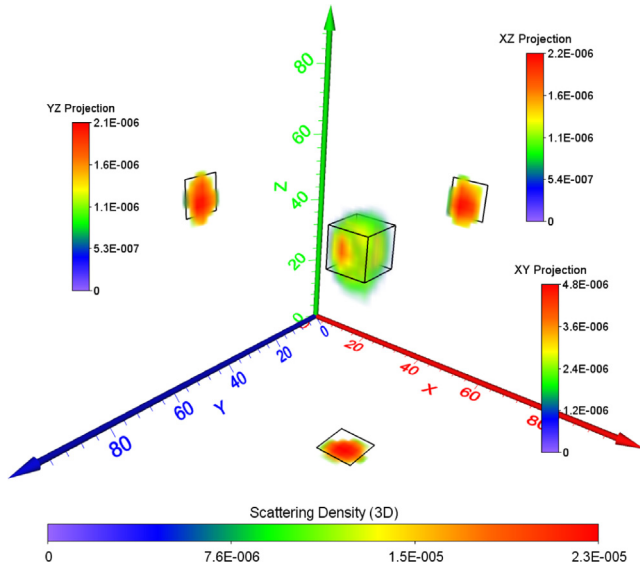


Fig. 18. Pb target (as seen in the left plot of Fig. 17) with normalized projections onto all 3 orthogonal planes. Shown also are the real dimensions of the lead target. (For interpretation of the references to color in this figure caption, the reader is referred to the web version of this paper.)

muons). Muons with momenta less than $0.5 \text{ GeV}/c$ are often stopped by the steel slabs before they reach the last detector super-layer. Consequently, they do not provide enough information for a momentum estimate via scattering and are not currently used in the analysis. A low-momentum estimate can be assigned in future analyses.

Fig. 15 shows the distribution of percent differences between the generated and reconstructed momenta (the “momentum residual”). A Gaussian fit was made to the central range of the distribution (shown as the red curve in Fig. 15) for which the mean value is -37% , and the width is 24% . Although a Gaussian fit gives a reasonable estimate of the momentum resolution for the majority of events, the momentum residual distribution is not

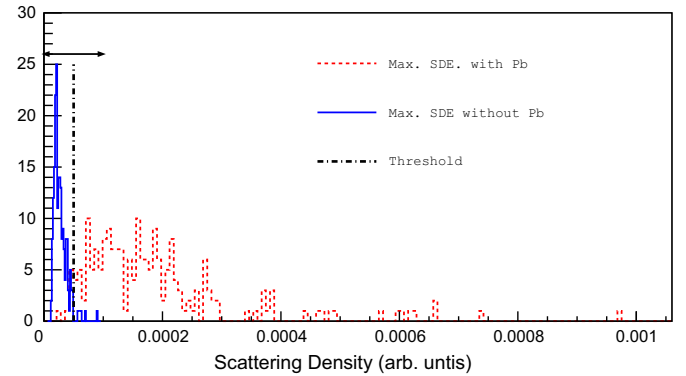


Fig. 19. Example of SDE distributions used to construct ROC curves.

symmetric, and therefore not Gaussian: there is a tail at larger values of the momentum residual. As a result, the mean of the whole distribution is actually slightly closer to zero (the ideal for an unbiased estimator): -28% . Table 1 shows the mean and RMS values of the momentum residual distributions binned by reconstructed momentum. As expected, the RMS is smallest for low momentum muons as they tend to have larger (and more easily measured) scattering angles; however, the bias is smallest for large momentum muons. The systematic underestimate of muon momenta can be corrected to provide an improved estimate.

4.3.2. Measured muon momentum spectrum

The momentum spectrum of reconstructed muons is investigated with no objects in the imaging volume. Any particle scattering that occurs is the result of interactions with the CRIPT apparatus. Fig. 16 shows the results of the momentum measurements, as well as a Monte Carlo simulation of the measurements. The shapes of the distributions are strongly influenced by the momentum-dependent reconstruction efficiency (Fig. 14) and the bias of the reconstructed momentum values (Table 1). The real data tend to have more large-angle scattering than the Monte

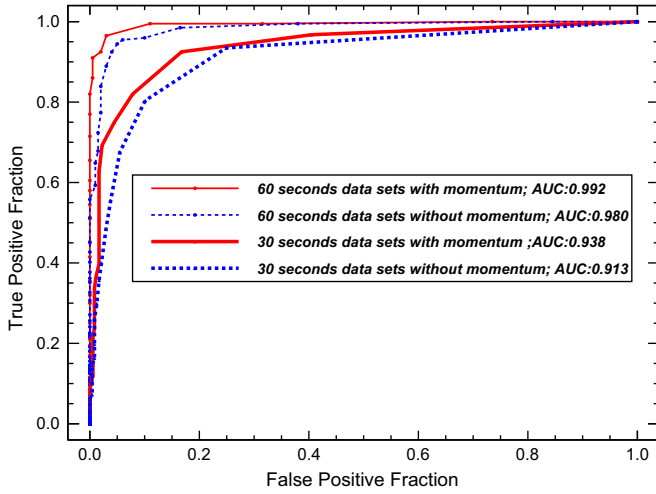


Fig. 20. Receiver operating characteristic curves for a lead target. The area under the curve (AUC) close to unity represents a high probability to detect high-Z material (in this case lead target) while maintaining a low false alarm rate.

Carlo so the reconstructed momentum distribution of the data is softer, on average.

4.4. Receiver operating characteristic (ROC) curves

In order to quantify how including momentum information improves CRIPT's ability to detect dense, high-Z material, a simple experiment was performed. A $20 \times 20 \times 20 \text{ cm}^3$ cube, constructed from lead bricks was placed in the centre of the imaging volume. The resulting reconstructed images of the cube are shown in Figs. 17 and 18.

The reconstruction method used to create the images is called scattering density estimation (SDE) which is described in detail in [22]. This software uses the measured point-of-closest-approach (PoCA) information from each pair of muon track segments in the UT and LT. The PoCA approximates the location (or three-dimensional voxel) where most of the scattering occurred. Using measurements of the three-dimensional scattering angle, σ_θ , and muon momentum, the scattering density of the material in a voxel can be defined as

$$\lambda = \frac{\sigma_\theta^2}{x} \left[\frac{\beta cp}{(\beta cp)_0} \right]^2 \quad (5)$$

where x is the path length of the muon in the material,⁵ βcp is the product of the muon speed and momentum and $(\beta cp)_0$ is the average speed times momentum for atmospheric muons.

As seen in Figs. 17 and 18, the lead target is readily identifiable. The dimensions and the location of the cube are well represented by the reconstructed image. The inset in Fig. 18 is the real boundaries of the lead target. It should be noted that no special alignment of the lead was performed with respect to the voxel locations. This means that the boundary of the lead/air interfaces fall not at the edges of voxels but rather near their centres. This causes the edges of the reconstructed image to be blurred and have a systematically lower scattering density. In Fig. 18, the scattering density scales for the three-dimensional (3D) voxels and the two-dimensional projections (XY, XZ, YZ) differ by almost an order of magnitude as the projected values are the average scattering densities of all the voxels along one axis; most of these voxels are empty so have scattering densities very close to zero. Detailed studies correlating reconstructed scattering densities to

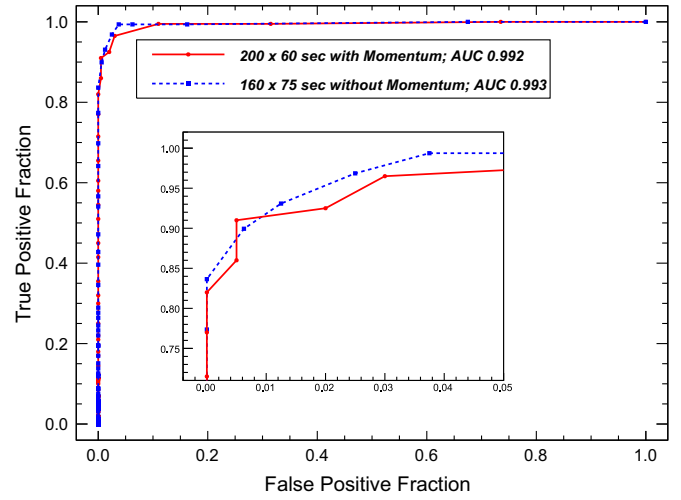


Fig. 21. Momentum estimation gains: reduced time-to-detect and larger area under the curve. Inset: zoom near 100% true positive fraction.

material densities and/or radiation lengths will be published in a forthcoming paper. In Fig. 17, the low scattering density “noise” which appears below the location of the lead block (looking like a blue “haze”) is due to multiple scattering caused by the 1.25 cm thick steel support plate.

ROC curves are used in many fields of research to make quantitative assessments of classification performance [24]. The procedure for generating the ROC curve is described here. A data set is divided into 100 (or more) subsets consisting of 30 or 60 s of muon data. The SDE method is applied to each subset independently and the maximum scattering density per subset is compiled into a histogram. The same analysis takes place for the two data sets being compared: (a) the set containing the 8000 cm^3 lead target and (b) the set containing no target. This analysis produces two distributions as seen in Fig. 19. A threshold is applied to the two distributions simultaneously and is incremented to step across the entire range of the distributions. At each step, the fractions of data on either side of the threshold are used to determine the following fractions: false positive, false negative, true positive, and true negative. These fractions are determined due to a priori knowledge of which distribution corresponds to which target. The ROC curves in this paper are constructed by plotting the true positive fraction against the false positive fraction at each step.

The importance of the momentum information is clear when one considers the effect on the true positive fraction (TPF) at small false positive fractions (FPFs); small FPF values are required for cargo-scanning in order to avoid unacceptably high false alarm rates. For the 60 s scan times and an FPF of 0.02, the TPF increases from 0.77 to 0.92 when momentum information is used (see Fig. 20). Another way of quantifying the impact of the momentum estimation is to consider the area under the curve (AUC) for each ROC curve. The AUC increases significantly when momentum information is added. Overall, the FPF is closer to the ideal value of 0.0 when the momenta of the muons are included.

Additional ROC curves were produced using the data without momentum estimation in order to determine how much extra scanning time would be required to obtain similar results to the 60 s scans with momentum estimation included. Using the AUC metric, it appears that an additional 15 s would be required to obtain similar results without momentum estimation (i.e. 75 s). The curves for this study are shown in Fig. 21.

It is important to note that the performance for high-density, high-Z material detection would be greatly enhanced by increasing the angular acceptance for muon tracking. CRIPT has a very

⁵ On a voxel-by-voxel basis.

limited angular acceptance as it is a proof-of-concept system, rather than an operational prototype. Only 24.6% of the muons that pass through the imaging volume pass through all layers of the UT and LT. Using muons at zenith angles closer to horizontal would also greatly improve the image resolution along the z-axis, and increase the muon statistics passing through all voxels, especially those on the edges of the imaging volume. With the current angular acceptance, the voxels on the edges have much lower statistics which leads to a higher FPF; this is an effect that has been noted previously [9].

5. Conclusion

The first muon scattering tomography system using plastic scintillator bars to track muons has been constructed and its capabilities successfully demonstrated. The performance of CRIPT's muon detectors based on detection efficiency and hit resolution (on average $\epsilon=97\%$ per plane, with an intrinsic hit resolution of 2.5 mm) are consistent with expectations. In addition to imaging a variety of objects of interest (details of which will be in a forthcoming paper), a quantitative study has been carried out to investigate the impact of including muon momentum measurements in the tomographic images. As expected, the momentum information improves the ability to detect high-density, high-Z material (in this case Pb). For a fixed time (60 s) and a fixed false positive fraction, the probability to detect a target increases significantly when momentum information is used. To our knowledge, this is the first demonstration of the use of direct muon momentum measurements in muon scattering tomography.

Acknowledgments

We would like to thank all those who have contributed in one way or another to the realization of this work, especially our colleagues from the Canadian Nuclear Laboratories (former Atomic Energy of Canada) in particular Dr. B. Sur, and the technical and machine shop staff at Carleton University's Science and Technology Centre, Advanced Applied Physics Solutions, and the National

Research Council of Canada's Model Shop. This work was supported by the Canadian Research and Technology Initiative through project CRTI 08-0214RD.

References

- [1] K. Borozdin, et al., *Nature* 422 (6929) (2003) 277.
- [2] W. Priedhorsky, et al., *Review of Scientific Instruments* 74 (10) (2003) 4294.
- [3] G. Jonkmans, et al., *Annals of Nuclear Energy* 53 (2013) 267.
- [4] G.R. Lynch, O.I. Dahl, *Nuclear Instruments and Methods in Physics Research Section B: Beam Interactions with Materials and Atoms* 58 (6) (1991) 6.
- [5] S. Pesente, et al., *Nuclear Instruments and Methods in Physics Research A* 604 (3) (2009) 738.
- [6] R. Barlow, et al., A drift chamber system for muon tomography, *Applied Nucleonics Forum*, Teeside, 2010.
- [7] M. Bogolyubskiy, et al., First test of cosmic ray muon tomography prototype being constructed at IHEP, in: 2008 IEEE Nuclear Science Symposium Conference Record, 2008, pp. 3381–3383.
- [8] D. Mahon, et al., *Nuclear Instruments and Methods in Physics Research A* 732 (2013) 408.
- [9] K. Gnava, et al., *Nuclear Instruments and Methods in Physics Research A* 652 (1) (2011) 16.
- [10] P. Baesso, et al., *Journal of Instrumentation* 8 (08) (2013) P08006.
- [11] F. Xing-Ming, et al., *Chinese Physics C* 38 (4) (2014) 046003.
- [12] M. Benettoni, et al., *Journal of Instrumentation* 8 (12) (2013) P12007.
- [13] M. Motoki, et al., *Astroparticle Physics* 19 (1) (2003) 113.
- [14] D.G. Michael, *Nuclear Instruments and Methods in Physics Research A* 596 (2) (2008) 190.
- [15] MINERvA Collaboration, The MINERvA Technical Design Report, 2006, MINERvA-doc-700-v28.
- [16] Hamamatsu (n.d.), Resources, (http://www.hamamatsu.com/resources/pdf/etd/H8804_TPMH1333E01.pdf), 2014 (retrieved June 2).
- [17] MIDAS (n.d.), (<http://midas.psi.ch/>), 2014 (retrieved June 2).
- [18] Vertilon (n.d.), (<http://www.vertilon.com/>), 2014 (retrieved June 2).
- [19] S. Agostinelli, et al., *Nuclear Instruments and Methods in Physics Research A* 506 (2003) 250; J. Allison, et al., *IEEE Transactions on Nuclear Science* NS-53 (2006) 270 <http://geant4.cern.ch>.
- [20] P.-L. Drouin, D. Waller, Muon Momentum Reconstruction Algorithms for the CRIPT Spectrometer, Defence Research and Development Canada, Ottawa, DRDC Ottawa TM 2011-210, 2011.
- [21] R. Carnegie, et al., *Nuclear Instruments and Methods in Physics Research A* 538 (1) (2005) 372.
- [22] V. Anghel, et al., Patent No. 2838656, Canada, 2012, December 13.
- [23] F. James, MINUIT: Function Minimization and Error Analysis, Long Writeup D506, CERN Program Library, 1994.
- [24] T. Fawcett, *Pattern Recognition Letters* 27 (8) (2006) 861.